Research Article | Vol. 31, No. 13 / 19 Jun 2023 / Optics Express 22170
Optics EXPRESS

High-efficiency upward radiation in a slow-light grating beam scanner

SANEYUKI SUYAMA AND TOSHIHIKO BABA*

Department of Electrical and Computer Engineering, Yokohama National University, 79-5 Tokiwadai, Hodogaya-ku, Yokohama 240-8501, Japan
baba-toshihiko-zm@ynu.ac.jp

Abstract: Slow-light grating (SLG) is used as a solid-state optical beam scanner, but the efficiency of conventional SLGs has been constrained by unwanted downward radiation. In this study, we developed a high-efficiency SLG consisting of through-hole grating and surface grating, which selectively radiates upward. Via the optimization using the covariance matrix adaptation evolution strategy, we designed a structure showing a maximum upward emissivity of 95% as well as moderate radiation rates and beam divergence. Experimentally, the emissivity was enhanced by 2–4 dB and the roundtrip efficiency was improved by 5.4 dB, which is significant in applications to light detection and ranging.

1. Introduction

Light detection and ranging (LiDAR), an image sensor that acquires surroundings in three dimensions, is currently gaining attention for its application in auto-driving, robots, mapping, among others [1]. LiDAR targeting middle and long distances are commonly equipped with a mechanical mirror for beam scanning, which constrains the size and performance of LiDAR. To solve this, mirror-less scanners exploiting Si photonics platform and mechanisms such as optical phased array (OPA) [2–4], focal plane array (FPA) [5,6], and slow-light grating (SLG) [7–9] have been developed. The former two requires ultra-large-scale photonic integration and complicated control, whereas these requirements are relaxed using SLG. As described in Fig. 1, SLG consists of a photonic crystal waveguide (PCW) with a shallow-etched surface grating, fabricated using the Si photonics wafer process. It radiates a slow-light mode of this waveguide into free space as a fan beam with narrow angular divergence $\delta\theta$ and a wide $\delta\phi$ in the longitudinal and lateral directions, respectively. Owing to the slow-light effect, it provides a scanning angular range $\Delta\theta$ wider than that in standard diffraction grating waveguides for a wavelength sweep range $\Delta\lambda$ and/or a refractive index change Δn induced thermo-optically.

In general, however, the upward emissivity ξ is only 50% due to downward radiation, when the grating waveguides are vertically symmetric. This results in a 6 dB loss during the transmission and reception of LiDAR. Conventional SLG is not completely symmetric due to the existence of the surface grating and upper air and lower substrate, but a 40% (2.2 dB) downward radiation loss and a 4.4 dB roundtrip loss have been calculated [8], which are significant in LiDAR applications. Besides, the change in the beam angle θ has modified the radiation rate α_{rad}, radiation efficiency η, and beam divergences $\delta\theta$ and $\delta\phi$, making the use of SLG complicated.

Thus far, a lower mirror [10,11] and multi-step structures [12–15] have been reported as high ξ grating waveguides, although they overall require complicated processes and/or a small dimension of <100 nm in their planer structures. In this paper, we propose and discuss an SLG structure composed of a through-hole grating and surface grating, which is much simpler to fabricate and suitable for high emissivity and efficiency. We also show the automatic optimization of the structure for high ξ and desired α_{rad} and their numerical simulation and experimental results.

#493704 https://doi.org/10.1364/OE.493704
Journal © 2023 Received 19 Apr 2023; revised 31 May 2023; accepted 11 Jun 2023; published 15 Jun 2023

Optics EXPRESS

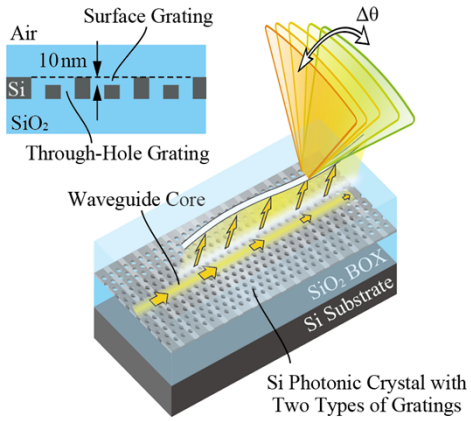

Fig. 1. Schematic of a single SLG beam scanner. For two-dimensional scanning, its array and a collimator lens are used.

2. Principle

Let us first discuss the principle of high upward emissivity. The through-hole grating is formed by modulating the diameter and location of holes in the PCW with a period of $2a$ for the PCW's lattice constant of a [16]. The surface grating is also formed on top of the PCW with a period of $2a$ [7].

Figure 2 shows simulation examples of light radiation from either the through-hole grating or the surface grating, which were obtained using the finite-difference time-domain (FDTD) method (calculation details are omitted as they only show the phenomena qualitatively). The through-hole grating radiates the guided mode into the upper and lower directions symmetrically with the same phase. On the other hand, the surface grating radiates with the opposite phases as the downward radiation suffers from a phase delay $\Delta\varphi \approx k_0 nd$ in the slab, where k_0 is the wave number in vacuum and n and d are the index and thickness of the slab, respectively. Assuming typical values such as the wavelength $\lambda = 1550$ nm, $n = 3.44$, and $d = 210$ nm, $\Delta\varphi$ is calculated to be almost the opposite phase 0.93π. Therefore, mixing these two cancels the downward radiation and enhances the upward one. The maximum upward emissivity is obtained when the intensities and locations of radiated light are coincided with each other, which needs the optimization of the two grating structures. Their intensities can be controlled by the modulation amplitude of the hole's diameter and location of the through-hole grating and by the etch depth of the surface grating. It consequently has an asymmetric planar structure along the PCW, which means that high efficiency is expected for a unique direction of light propagation; the phase relation is inverted and the upward emissivity is rather reduced for the opposite light propagation.

The far-field beam profile $Y(\theta)$ is expressed as

$$Y(\theta) \propto \left| \int_0^L \sqrt{\xi \alpha_{\mathrm{rad}} P_0 \exp[-(\alpha_{\mathrm{loss}} + \alpha_{\mathrm{rad}})y]}\ \exp(-jk_0 y \sin\theta) dy \right|^2 \tag{1}$$

where L is the SLG's length, P_0 is the incident power, α_{loss} is the propagation loss caused by the imperfection of the waveguide, and y is the axis of light propagation in the PCW. The radiation efficiency η is given by

$$\eta = \int_0^L \xi \alpha_{\mathrm{rad}} \exp[-(\alpha_{\mathrm{rad}} + \alpha_{\mathrm{loss}})y] dy. \tag{2}$$

Optics EXPRESS

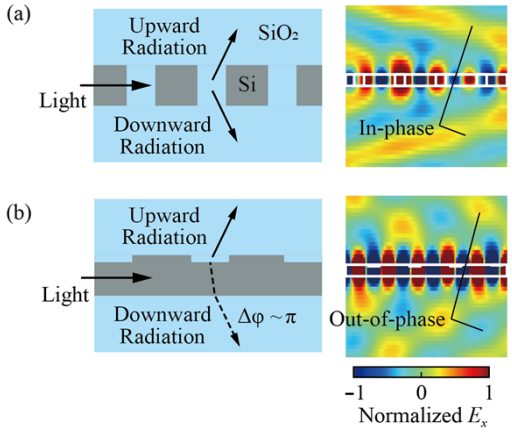

Fig. 2. Cross-sectional model (left) of (a) through-hole grating and (b) surface grating and finite-difference time-domain (FDTD) simulations of light radiation (right). In the simulation, polarization is assumed to be perpendicular to the paper surface (E_x).

3. Optimization

In simulating light propagation, we fixed the Si slab thickness to 210 nm and surface grating depth to 10 nm and assumed SiO_2 upper and lower cladding (holes are also filled with SiO_2). Then, we first modeled a conventional SLG structure [7] having a uniform hole diameter $2r = 208$ nm, lattice constant $a = 394$ nm, and third-row shift $s = 95$ nm. We simulated using Ansys Lumerical FDTD with its middle accuracy setting (Accuracy 2) and a periodic boundary condition of $2a$ period. An optical pulse of transverse-electric polarization was excited in the Si slab, and average powers at planes 3.5 μm above and below the Si slab were counted to extract ξ. The α_{rad} was estimated from the time constant τ of the guided mode, the group index n_g obtained from the photonic band, and the relation $\alpha_{rad} = n_g/c\tau$ (c is the velocity in vacuum). The divergence $\delta\phi$ (full-width at half maximum: FWHM) of the fan beam was calculated from the spatial Fourier transformation of the in-plane distribution of the modal electric field. For these calculations, refractive indices of materials were referred to those in a library of used software.

For structural optimization, we used the covariance matrix adaptation evolution strategy (CMA-ES) [17]. In this algorithm, structural models are randomly generated with multiple optimization parameters in a normal distribution, and calculations, evaluations, and generation update are repeated to converge the structure to an optimum one. Compared with other similar algorithms, it only needs a limited number of hyper-parameters and effectively suppresses to fall into local minima. In this calculation, the diameter and the x and y locations of six circular holes on the first to third rows in a unit cell and the widths at the start and end points, the location of the start point, the length, and the angle of the surface grating were chosen as 23 optimization parameters. Only upward emissivity ξ is used as the target value to be enhanced, and α_{rad} was controlled close to 100 dB/cm afterward by slightly shifting the start point of the grating, as how this point is located close to the waveguide core dominates α_{rad}. The number of models in each generation of the optimization was 25, whereas the number of generations was 50. Using 25 standard personal computers (Windows 10, Intel Core-i7-6700), the calculation time was 30 min for each generation, which took 25 h in total.

Figure 3(a) shows planar structures of SLG before (black dashed line) and after (red solid line) optimization, where light is assumed to propagate from left to right. After the optimization, the diameter and location of each hole were changed slightly, and the grating was tilted by 5.1°. Figure 3(b) displays the simulation results of cross-sectional light propagation for this structure

Optics EXPRESS

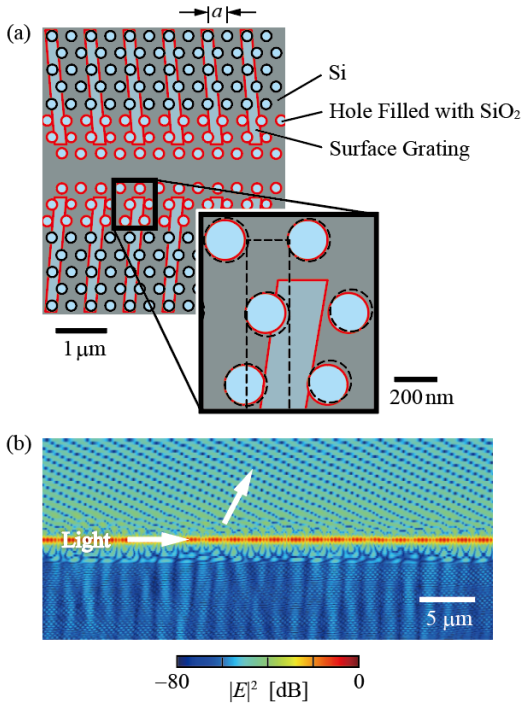

Fig. 3. (a) Plain view of the optimized SLG structure. Black dashed line and red solid line show before and after optimization, respectively. (b) Simulated cross-sectional distribution of light radiation from optimized SLG.

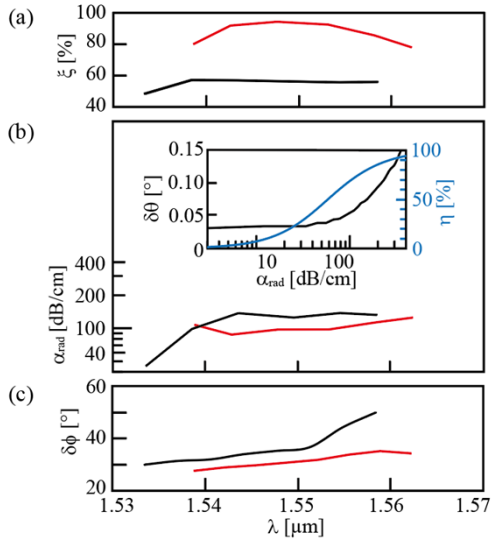

Fig. 4. The comparison of theoretical characteristics before (black) and after (red) optimization. (a) Upward emissivity ξ. (b) Radiation rate α_{rad}. (c) Lateral divergence of fan beam $\delta\phi$ (FWHM). The inset in (b) shows the longitudinal divergence of fan beam, $\delta\theta$ (FWHM), and efficiency η for α_{rad}, assuming $\xi = 95\%$, $\alpha_{loss} = 65$ dB/cm and $L = 0.15$ cm.

Optics EXPRESS

using rough accuracy (Accuracy 1) of the used software. The center intense line shows the slow light mode, and the selective upward radiation is confirmed. The complicated pattern of the downward radiation is considered as residual components of the destructive interference. The results were consistent even when the upper air and lower substrate were exchanged into SiO_2. This means that the reflection from air and substrate boundaries does not significantly contribute to the upward radiation, but the SLG structure itself does. The similar behaviors can be seen in multistep grating couplers showing a high upward emissivity [18,19].

Figure 4 summarizes the spectral characteristics of ξ, α_{rad}, and $\delta\phi$ in the slow-light operating band. The shift of operating band after the optimization is caused by the slight change in the photonic band profile. The ξ is enhanced from 60% (2.2 dB loss) to maximally 95% (0.2 dB loss), and >80% (<1.0 dB) is maintained over the operating band. After the optimization, α_{rad} ranges from 80 to 120 dB/cm. The $\delta\phi$ ranges from 27°–35°, which is not a severe divergence for the beam collimation using a lens for two-dimensional beam scanning. The inset of Fig. 4(b) shows $\delta\theta$ and η calculated for α_{rad} using Eqs. (1) and (2). We can expect $\eta = 60\%$ and $\delta\theta = 0.04°$ when $\xi = 95\%$, $\alpha_{rad} = 85$ dB/cm, $\alpha_{loss} = 65$ dB/cm, and $L = 0.15$ cm.

4. Experiment

In the fabrication, we used 200-mm-diameter silicon-on-insulator wafer process including KrF excimer laser stepper exposure, for which the feature size for the processing of the Si layer was reduced to less than 150 nm using a phase shift mask. The thickness and size of each element were the same as those assumed in the simulation. Figure 5 shows a scanning electron micrograph (SEM) of the optimized SLG. The shallow surface grating and small modulation of hole diameter and location in the $2a$ period are observed. The length of the SLG, L, was set at 0.15 cm, which was also assumed in the calculation. On each side of the photonic crystal waveguide, 12 rows of holes were arranged, and the total width of the SLG was 8.3 μm.

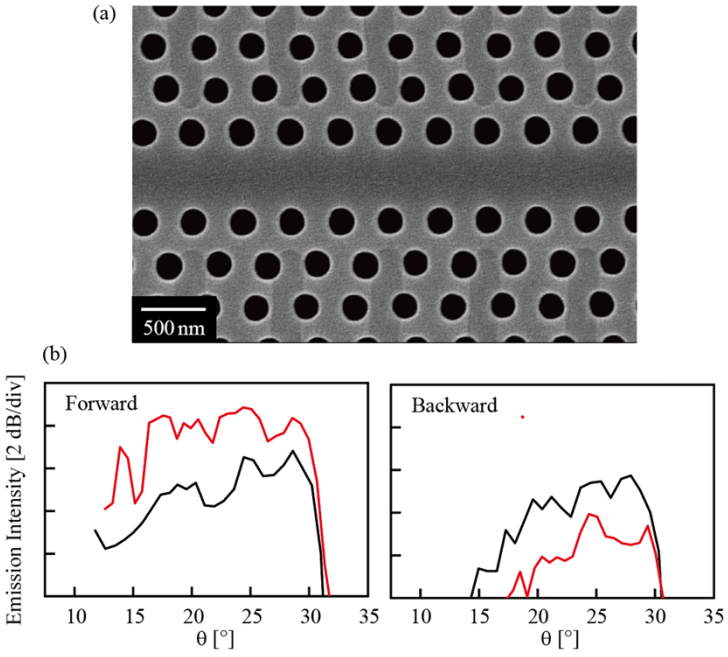

Fig. 5. (a) SEM picture of the fabricated SLG. (b) Radiation power versus beam angle characteristics. Black and red lines are before and after optimization, respectively.

Optics EXPRESS

In the measurement, TE-polarized laser light from a tunable source (Santec TSL-550) was coupled via a polarization-maintaining fiber with a lens module into an on-chip Si spot-size converter (SSC). By measuring the decay of the guided mode along the SLG using a near-field microscope and InGaAs camera, the value of $\alpha_{rad} + \alpha_{loss}$ was evaluated to be 140–150 dB/cm in the –3 dB bandwidth of slow light. Directly detecting upward radiated light using an optical power meter, the insertion loss from the fiber to the power meter directly detecting upward radiation was measured to be 7.3–8.9 dB. Thereafter, we separately evaluated the fiber–SSC coupling loss to be 3.6 dB, the propagating loss of the Si wire waveguide to be 0.2 dB (2 dB/cm and 0.1 cm length), Si wire–SLG transition loss for early optimized tapered transition [18] to be 0.7 dB, and the insertion loss of SLG to be 2.8–4.4 dB. This lowest value means $\eta = 54\%$, which is explained by assuming $\xi = 86\%$. To improve η to higher than 80% (<1 dB loss), for example, α_{loss} must be suppressed to 17 dB/cm for $\alpha_{rad} = 100$ dB/cm. As the modulation of hole diameter and location in the through-hole grating produces some amount of radiation, we cannot evaluate α_{loss} independently of α_{rad}, even when removing the surface grating. However, $\alpha_{loss} < 17$ dB/cm is not considered a serious value for a conventional PCW with a uniform hole diameter; we have evaluated $\alpha_{loss} < 10$ dB/cm when using other foundry services with an ArF stepper exposure.

The radiated fan beam was further evaluated by projecting it on a screen. Figure 5(b) compares the summed beam power with the change in θ before and after the optimization. The small fluctuation might have been caused by the nonuniform propagation characteristics of the PCW and/or the influence of the reflection at air and substrate boundaries. In the forward direction,

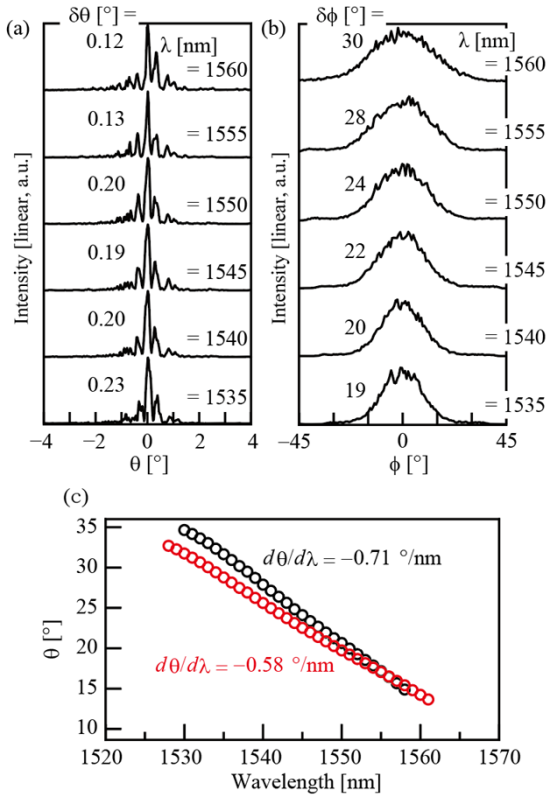

Fig. 6. Beam characteristics. (a) θ profile. Sidelobe was not counted in this evaluation of δθ. (b) ϕ profile. (c) Wavelength sensitivity of θ. Black and red lines in (c) are the same as those in Fig. 5(b).

Optics EXPRESS

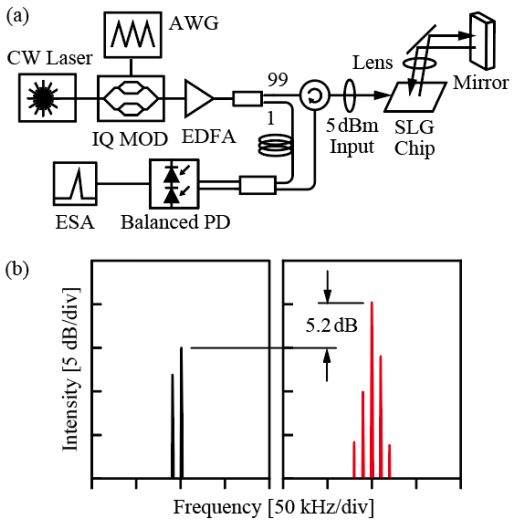

Fig. 7. FMCW LiDAR experiment. (a) Setup. (b) Measured beat spectrum providing the target range. Black and red lines in (b) are the same as those in Fig. 5(b).

which was expected to provide high efficiency, the radiation intensity was enhanced by 2–4 dB (2.3 dB in average over the slow-light band), as compared with that before the optimization. This corresponds to an improvement of S/N for roundtrip light when the device is applied to LiDAR. In the opposite direction, the radiation power was reduced by 4–5 dB, compared with that in the forward direction. Then, the upward emissivity in the forward direction is estimated to be 2.0–2.5 dB higher than 50%, i.e., $\xi = 79$–89%. This value is consistent with the calculated values in Fig. 4 and the above assumption for evaluating η.

Figure 6(a) shows the beam profile in the θ and ϕ directions. The longitudinal divergence $\delta\theta$ was as wide as 0.12°–0.23° even neglecting sidelobes, which is much larger than 0.04° estimated from the inset of Fig. 4(b) with the measured $\alpha_{rad} + \alpha_{loss}$. This must be caused by the nonuniformity and disordering of the fabricated SLG, which is also understood from the relatively large sidelobe. This will be improved by using a more advanced foundry service exploiting an ArF stepper. Figure 6(b) also shows $\delta\phi$ to be 19°–30°, but we also observed that these values were sensitively to the hole size. For slightly smaller holes, which shifted the operating wavelength range to 10 nm longer, $\delta\phi$ increased up to 38°. Figure 6(c) summarizes the θ–λ characteristics. After the optimization, the wavelength sensitivity of θ was reduced from 0.71°/nm to 0.58°/nm, meaning the slow-light effect was reduced. The latter sensitivity value is obtainable for $n_g = 13$, which is smaller than the expected value of 15–16. In general, n_g depends on the hole diameter, and the decrease of n_g can be explained by the diameter of the fabricated SLG, which is 5 nm smaller than the designed value.

We finally evaluated the roundtrip efficiency of the SLG from the range signal intensity of frequency-modulated continuous-wave (FMCW) LiDAR. As shown in Fig. 7(a), laser light is first frequency-modulated using $LiNbO_3$ in-phase and quadrature-phase (I-Q) single sideband modulator driven by an arbitrary waveform generator. The frequency of the sinusoidal signal was changed with a sawtooth function whose frequency bandwidth was 10 GHz and a sweep period of 100 µs. Then, the light was amplified using erbium-doped fiber amplifier and divided into signal and reference arms. The signal light of 5 dBm in the fiber was coupled into the SLG chip and transmitted to a mirror. The reflected light was detected by the same SLG and sent to a coherent receiver through an optical circulator. In the receiver, the signal light was mixed with reference light via a 2×2 coupler and was detected by balanced photodiodes (PD) to observe a

Optics EXPRESS

beat signal in the electrical spectrum analyzer, corresponding to a target range. When $\theta = 20°$ and the range $R = 3.2$ m, the beat spectrum was obtained, as shown in Fig. 7(b). Due to the enhanced ξ, the beat spectrum intensity was enhanced by 5.2 dB, which can be explained by the enhanced radiation efficiency mentioned earlier.

5. Conclusion

In this study, we proposed and demonstrated an SLG beam scanner structure that has high upward emissivity ξ and radiation efficiency η, attributed to the destructive interference of downward radiation between the through-hole and surface gratings. These gratings were optimized using CMA-ES evolutionary algorithm, and the upward emissivity finally reached 95%. In the experiment, radiation from SLG increased by 2–4 dB and FMCW LiDAR signal increased by 5.2 dB, compared to those of conventional SLG. The wavelength sensitivity lower than the conventional one due to a lower group index must be improved by further optimizations. Moreover, radiation efficiency was evaluated to be 52%, which was explained by a waveguide loss of 65 dB/cm. If the loss value is reduced to 17 dB/cm, which is a practical value when we use a more advanced foundry service with an ArF stepper, the efficiency will be enhanced to 80%.

Funding. New Energy and Industrial Technology Development Organization (JPNP14004); Japan Society for the Promotion of Science (22H00299).

Disclosures. The authors declare no conflicts of interest.

Data availability. Data underlying the results presented in this paper are not publicly available at this time, but may be obtained from the authors upon reasonable request.

References

1. Y. Li and J. Ibanez-Guzman, "Lidar for autonomous driving: the principle, challenges and trends for automotive lidar and perception systems," IEEE Signal Process. Mag. **37**(4), 50–61 (2020).
2. C. V. Poulton, M. J. Byrd, P. Russo, B. Moss, O. Shatrovoy, M. Khandaker, and M. R. Watts, "Coherent LiDAR with an 8,192-element optical phased array and driving laser," IEEE J. Sel. Top. Quantum Electron. **28**(5: Lidars and Photonic Radars), 1–8 (2022).
3. T. Kim, P. Bhargava, C. V. Poulton, J. Notaros, A. Yaacobi, E. Timurdogan, C. Baiocco, N. Fahrenkopf, S. Kruger, T. Ngai, and Y. Timalsina, "A single-chip optical phased array in a wafer-scale silicon photonics/CMOS 3D-integration platform," IEEE J. Solid-State Circuits **54**(11), 3061–3074 (2019).
4. S. Chung, H. Abediasl, and H. Hashemi, "A monolithically integrated large-scale optical phased array in silicon-on-Insulator CMOS," IEEE J. Solid-State Circuits **53**(1), 275–296 (2018).
5. C. Rogers, A. Y. Piggott, D. J. Thomson, R. F. Wiser, I. E. Opris, S. A. Fortune, A. J. Compston, A. Gondarenko, F. Meng, X. Chen, G. T. Reed, and R. Nicolaescu, "A universal 3D imaging sensor on a silicon photonics platform," Nature **590**(7845), 256–261 (2021).
6. X. Zhang, K. Kwon, J. Henriksson, J. Luo, and M. C. Wu, "A large-scale microelectromechanical-systems-based silicon photonics LiDAR," Nature **603**(7900), 253–258 (2022).
7. H. Ito, Y. Kusunoki, J. Maeda, D. Akiyama, N. Kodama, H. Abe, R. Tetsuya, and T. Baba, "Wide beam steering by slow-light waveguide gratings and a prism lens," Optica **7**(1), 47 (2020).
8. T. Tamanuki, H. Ito, and T. Baba, "Thermo-optic beam scanner employing silicon photonic crystal slow-light waveguides," J. Lightwave Technol. **39**(4), 904–911 (2021).
9. T. Baba, T. Tamanuki, H. Ito, M. Kamata, R. Tetsuya, S. Suyama, H. Abe, and R. Kurahashi, "Silicon photonics FMCW LiDAR chip with a slow-light grating beam scanner," IEEE J. Sel. Top. Quantum Electron. **28**(5: Lidars and Photonic Radars), 1–8 (2022).
10. D. Taillaert, P. Bienstman, and R. Beats, "Compact efficient broadband grating coupler for silicon-on-insulator waveguides," Opt. Lett. **29**(23), 2749–2751 (2004).
11. D. Benedikovic, P. Cheben, J. H. Schmid, D. Xu, B. Lamontagne, S. Wang, J. Lapointe, R. Halir, A. O.- Moñux, S. Janz, and M. Dado, "Subwavelength index engineered surface grating coupler with sub-decibel efficiency for 220-nm silicon-on-insulator waveguides," Opt. Express **23**(17), 22628–22635 (2015).
12. T. Watanabe, M. Ayata, U. Koch, Y. Fedoryshyn, and J. Leuthold, "Perpendicular grating coupler based on a blazed antiback-reflection structure," J. Lightwave Technol. **35**(21), 4663–4669 (2017).
13. M. Raval, C. V. Poulton, and M. R. Watts, "Unidirectional waveguide grating antennas with uniform emission for optical phased arrays," Opt. Lett. **42**(13), 2563–2566 (2017).
14. A. Michaels and E. Yablonovitch, "Inverse design of near unity efficiency perfectly vertical grating couplers," Opt. Express **26**(4), 4766–4779 (2018).

Optics EXPRESS

15. B. Chen, Y. Li, L. Zhang, Y. Li, X. Liu, M. Tao, Y. Hou, H. Tang, Z. Zhi, F. Gao, X. Luo, G. Lo, and J. Song, "Unidirectional large-scale waveguide grating with uniform radiation for optical phased array," Opt. Express **29**(13), 20995–21010 (2021).
16. H. Abe, M. Takeuchi, G. Takeuchi, H. Ito, T. Yokokawa, K. Kondo, Y. Furukado, and T. Baba, "Two-dimensional beam-steering device using a doubly periodic Si photonic-crystal waveguide," Opt. Express **26**(8), 9389–9397 (2018).
17. N. Hansen, "The CMA Evolution Strategy: A Tutorial," arXiv, arXiv:1604.00772 (2016).
18. D. Bendikovic, C. Alonso-Ramos, S. Guerber, X. Le Roux, P. Cheben, C. Dupre, B. Szelag, D. Fowler, E. Cassan, D. Marris-Morini, C. Baudot, F. Boeuf, and L. Vivien, "Sub-decibel silicon grating couplers based on L-shaped waveguides and engineered subwavelength materials," Opt. Express **27**(18), 26239–26250 (2019).
19. R. Guo, S. Zhang, H. Gao, G. S. Murugan, T. Liu, and Z. Cheng, "Blazed subwavelength grating coupler," Photonics Res. **11**(2), 189–195 (2023).